Journal of Physics D: Applied Physics

PAPER

Optimization of pyroelectric figures of merit via magnesia doping in lithium tantalate single crystal

To cite this article: Feng Tang *et al* 2018 *J. Phys. D: Appl. Phys.* **51** 395101

IOP Publishing

Journal of Physics D: Applied Physics

J. Phys. D: Appl. Phys. **51** (2018) 395101 (7pp)

https://doi.org/10.1088/1361-6463/aad88d

Optimization of pyroelectric figures of merit via magnesia doping in lithium tantalate single crystal

Feng Tang[1], Siwei Long[1], Xin Yang[1], Mingming Yang[1], Jiliang Quan[1], Shaopeng Lin[2], Decai Ma[2], Yunzhong Zhu[2] and Biao Wang[1,2]

[1] State Key Laboratory of Optoelectronic Materials and Technologies/Institute of Optoelectronic and Functional Composite Materials, School of Physics and Engineering, Sun Yat-sen University, Guangzhou 510275, People's Republic of China

[2] Sino French Institute of Nuclear Engineering and Technology, Sun Yat-sen University, Zhuhai 519082, People's Republic of China

E-mail: zhuyzh7@mail.sysu.edu.cn (Y Zhu) and wangbiao@mail.sysu.edu.cn (B Wang)

Received 31 January 2018, revised 27 July 2018
Accepted for publication 7 August 2018
Published 21 August 2018

Abstract

This paper reports a series of experiments and optimization based on pyroelectric figures of merit (FoMs), which demonstrate that the proper doping of magnesia (MgO) can improve the thermal performance of lithium tantalate ($LiTaO_3$) in infrared sensors. Starting with MgO-doped $LiTaO_3$ grown by the Czochralski method, the heat capacity, pyroelectric coefficients and dielectric parameters of these single crystals are then investigated systematically. By considering the ultraviolet and infrared spectra, the variation of the electrical parameters and the occupation mechanism of MgO doping could be explained. It is found that the dopant increases the Curie temperature and broadens the operating temperature of pyroelectric devices. Notably, compared with congruent $LiTaO_3$, when the doping concentration reaches 5 mol%, the corresponding voltage responsivity and specific detectivity FoMs are enhanced by ten and two times, respectively.

Keywords: lithium tantalate, figures of merit, pyroelectric coefficient, dielectric property, Curie temperature

(Some figures may appear in colour only in the online journal)

1. Introduction

Pyroelectric materials are widely investigated for thermal imaging and infrared sensors [1–5]. Here, it is reported that temperature changes undergone by a pyroelectric crystal lead to opposite surface charges accumulating along the polarization direction that extends across the thickness of the crystal [6]. This phenomenon is further quantified as the pyroelectric coefficient $p = \partial P_S/\partial T$, which implies that the working temperature (T) could oscillate the spontaneous polarization (P_S) of pyroelectric materials [7]. In a standard pyroelectric measurement system, the required temperature oscillation is usually achieved via thermal radiation or conduction [8–10]. The thermal conduction method, also known as the dynamic method [10], possesses two advantages: convenient temperature control and charge collection. Specifically, when the electrodes of the pyroelectric single crystal are linked in an open circuit, a programmed temperature oscillation could induce current flow. The current stemming from the pyroelectric charge is given as $I = pA\,\mathrm{d}T/\mathrm{d}t$ (where A is the electrode area and $\mathrm{d}T/\mathrm{d}t$ is the rate of temperature change) [9].

The majority of existing literature related to pyroelectricity focuses on improving the coefficient p of the specific material. However, a high pyroelectric coefficient does not ensure excellent thermal performance [11]. In addition to the coefficient, a low dielectric loss tangent [12, 13] and low permittivity [13, 14] are also required. A high Curie temperature and stable chemistry are also essential to obtain acceptable pyroelectric performance over a wide temperature range and diverse working environment. For instance, due to their low Curie temperature, water solubility, chemical instability issues and environmental pollution problems, common pyroelectric materials such as TGS, PVDF, PT and PZT [15–18] cannot meet the demanding requirements of complex working environments. Hence, it is vital to find a robust pyroelectric material with both high-temperature stability and excellent pyroelectric performance.

To solve this problem, lithium tantalite ($LiTaO_3$, LT) and lithium niobate ($LiNbO_3$, LN) are considered [19]. Both LT and LN are known to have a high Curie temperature. Specifically, compared with LN, LT possesses a relatively low Curie temperature (665 °C) but much higher pyroelectric coefficient (1.7×10^{-4} C m^{-2} K^{-1}) [11]. To estimate the practical performance of this pyroelectric material, pyroelectric figures of merit (FoMs) can be referenced [11, 20, 21]. In infrared sensors, two types of FoMs are used to evaluate the performance: voltage responsivity (F_V) and specific detectivity (F_D),

$$F_V = p/C_P\varepsilon_r\varepsilon_0 \tag{1}$$

$$F_D = p/C_P(\varepsilon_r\varepsilon_0 \tan\delta)^{1/2}, \tag{2}$$

where C_p represents the volumetric specific heat capacity, ε_r is the relative dielectric constant, ε_0 is the permittivity of free space and tanδ is the dielectric loss [22].

In this paper, seven doped LT single crystals are grown from congruent melt with different Mg doping concentrations (0–6.0 mol%) by the Czochralski method (CZ). Infrared and ultraviolet spectra were recorded to determine the occupation site of the dopant. Then, based on the effect of Mg doping on the spontaneous polarization and the dipole moment of LT single crystals, the variation on the pyroelectric coefficient and permittivity could be explained. Combining the above results, we find that the pyroelectric FoMs are enhanced dramatically and the working temperature is also widened.

2. Materials and methods

In our experiment, Li_2CO_3 (4N purity) and Ta_2O_5 (4N purity) powders were mixed with a molar ratio of Li/Ta = 0.951. MgO powders (5N purity) were added to obtain doping concentrations of 0, 1, 2, 3, 4, 5 and 6 mol% (defined as CLT, 1-LT, 2-LT, 3-LT, 4-LT, 5-LT and 6-LT). The raw powders were mixed and ball milled to achieve a uniform mixture. Each mixture was heated to 1250 °C for 24 h in a muffle furnace. Then, single crystals were grown by a CZ furnace (as shown in figure 1(a)) in a nitrogen–oxygen gas mixture (98% N_2 and 2% O_2). The growth direction was the z-axis [0 0 1], using rotation and pulling rates of 6–15 rpm and 0.5–1.0 mm h^{-1}, respectively. Then the as-grown crystals were annealed and poled to a single domain state. Finally, as shown in the inset of figure 1(b), the crystals were cut into z-wafers, polished on both sides, and Au electrodes were deposited by electron beam evaporation (EB 450). X-ray rocking curve (Bruker D8) was used to check the crystallinity [23] in several square millimeters of the wafer. As shown in figure 1(b), a single diffraction peak with the full width at half maximum of 33.696 arcsec was obtained from the 5-LT wafer. The narrow and symmetric peak, located at 19.425°, suggested that the LT wafer was a perfect single crystal. A Parttulab HDMS and an Agilent E4980A precision LCR meter were used to measure the dielectric constant and dielectric loss under different temperatures (50 °C–350 °C) and continuously changing frequencies (0.1–100 kHz). The –OH absorption spectra of Mg:LT wafers were obtained at room temperature using a Fourier transform infrared (IR) spectrometer. In addition, the dopant occupation site was investigated by a UV–vis–NIR spectrophotometer (Lambda 950) as well. Changes in the Curie temperatures (T_C) and specific heat capacity for different doping concentrations was monitored using differential scanning calorimetry (DSC-204F1, Phoenix). In this work, the dynamic method was used to measure the pyroelectric coefficient, using a test platform presented in our previous work [22]. Specifically, the temperatures were controlled by a Linkam T95 together with a HFS600E stage, and the pyroelectric current across the single crystal was measured by a Keithley 6485 picoammeter with the accuracy of 0.4%.

3. Results and discussion

The voltage responsivity and specific detectivity of pyroelectric infrared sensors not only depend on the pyroelectric coefficient, but the dielectric constant, dielectric loss and heat capacity of the specific material. In this section, we will provide detailed illustrations of all relevant experimental results along with site occupation analysis based on the infrared and ultraviolet spectra and the corresponding variation of spontaneous polarization and electric dipole moment. Then, in the last part of this section, we will evaluate dopant and temperature-based pyroelectric FoM results and provide quantitative insight into the improvement of metrics related to FoMs.

3.1. Infrared and ultraviolet spectra

Figure 2(a) shows the original IR transmission spectra (inset) and the collection of –OH stretching vibration [24] of as-grown crystals with different MgO doping concentrations. When the Mg^{2+} concentration is below 3 mol%, the peak position gradually shifts to a longer wavelength. However, when it exceeds 4 mol%, the peak position shifts back slightly to a shorter wavelength. The fundamental optical absorption edge of ultraviolet (UV edge) spectra can also be used to establish the location of impurities in the crystal lattice. Figure 2(b) shows the UV spectra and the collection of absorption edges ($\alpha = 20$ cm^{-1}) for the seven as-grown crystals. One can see that as the doping concentration is increased from 0 to 3 mol%, the absorption edge shifts to a shorter wavelength, then returns sharply to 4 mol%. After that, as the doping concentration increases, again, the absorption edge shifts back to a shorter wavelength.

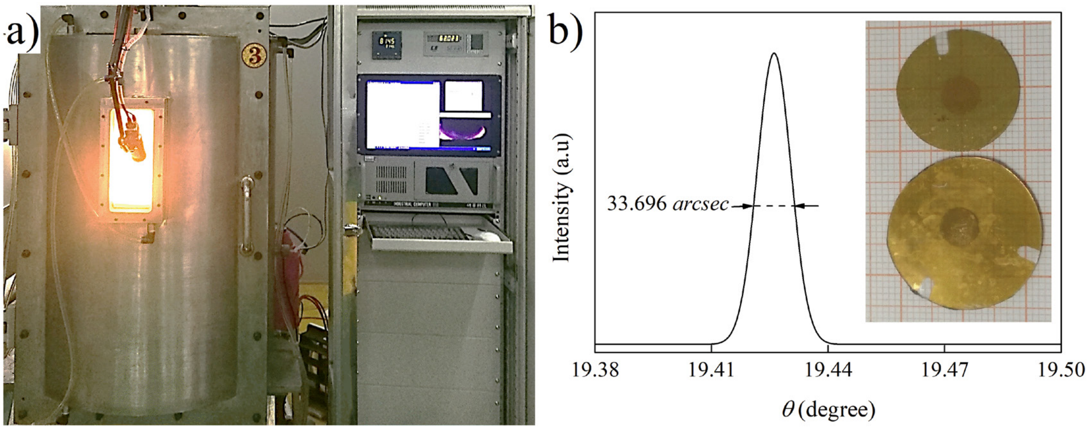

Figure 1. (a) The CZ single crystal growth furnace. (b) The c-ray rocking curve of 5-LT wafer, and the full width at half maximum (FWHM) is 33.696 arcsec. The *inset* presents the Au deposited LT wafers.

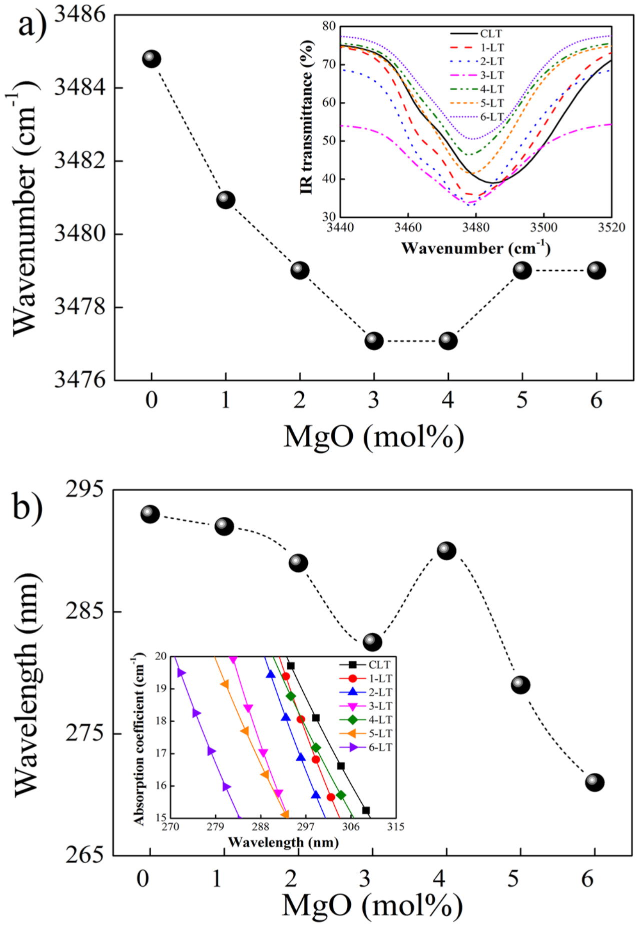

Figure 2. (a) The –OH absorption peak position as a function of Mg concentration in Mg:LT crystals, and the original IR transmission spectra of all samples are presented in the *inset*. (b) The UV absorption edge position of Mg:LT crystals as a function of Mg concentration, and the UV absorption edges of all samples are presented in the *inset*.

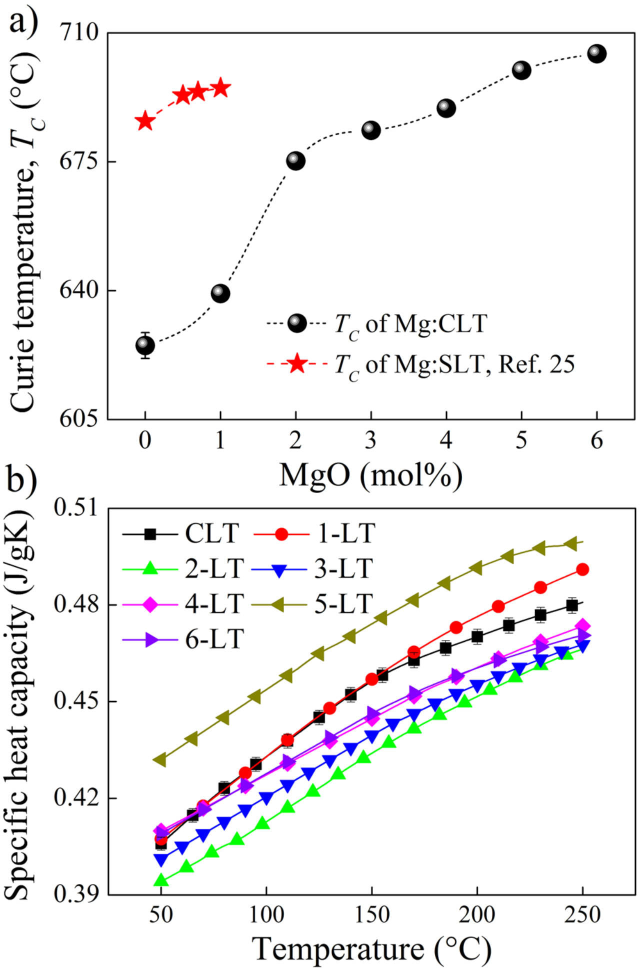

Figure 3. (a) The relationship between the Curie temperature (T_C) and Mg doping concentration, the red line represents the Curie temperature of Mg:SLT in [25]. (b) The specific heat capacities (C) of Mg:LT are measured at 50 °C–250 °C. (a) Reprinted from [25], Copyright (2006), with permission from Elsevier.

3.2. Curie temperature

Curie temperature (T_C) is the temperature where the ferroelectric phase transforms to the nonpyroelectric paraelectric phase. Since the pyroelectricity disappears in the paraelectric phase, and a high T_C is required for most applications, then maintaining the ferroelectric phase is a prerequisite of the LT pyroelectric wafer. Figure 3(a) shows the Curie temperature of all the samples. One can find that, in our Mg:LT single crystals, the Curie temperature gradually increases with Mg doping. However, the dopant has little influence on the T_C of the stoichiometric LT (SLT) [25].

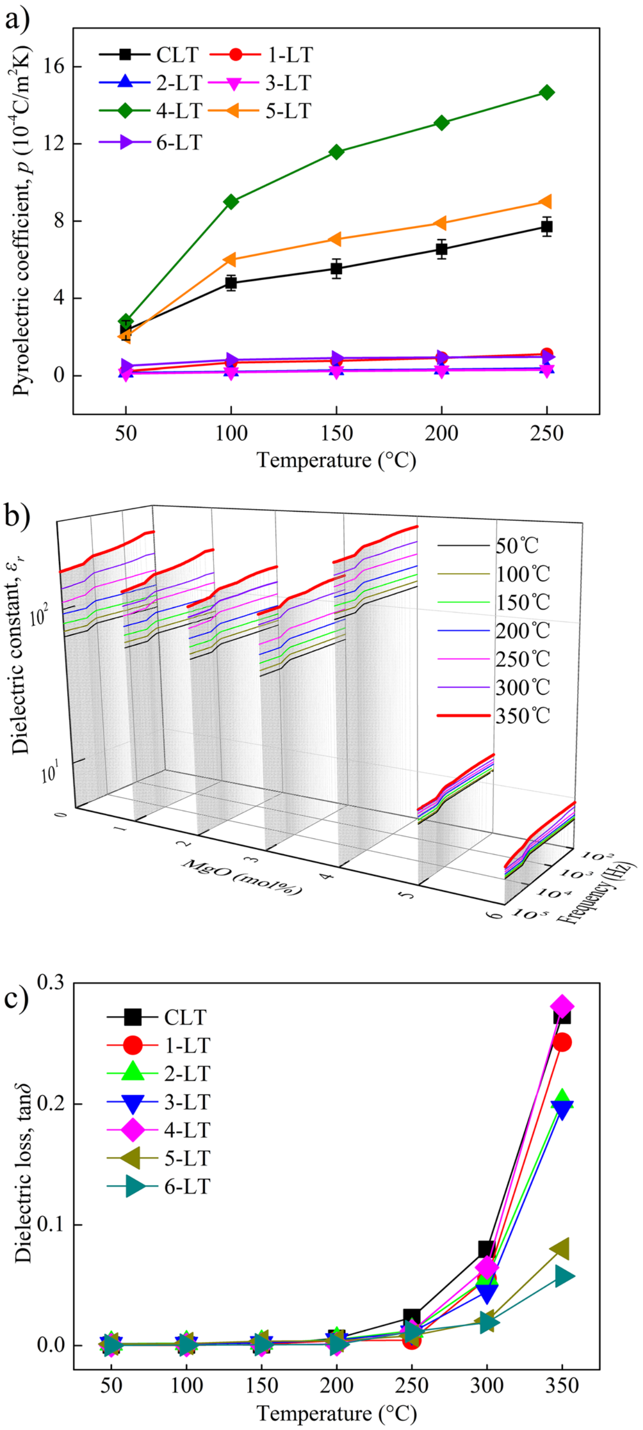

Figure 4. (a) The pyroelectric coefficients of seven samples are measured at 50 °C–250 °C. (b) The relative dielectric constants variation of seven samples under different temperatures (50 °C–350 °C) and frequencies (0.1–100 kHz). (c) The dielectric loss of all samples in various temperature at 1 kHz.

3.3. Specific heat capacity

In order to evaluate the specific detectivity potential and the voltage responsivity of a pyroelectric sensor, the specific heat capacity is needed. As shown in figure 3(b), the heat capacities of all the samples are measured from 50 °C–250 °C. The overall data tend to increase with the working temperature and display a small dependence on dopant level. It should be noted that the measured heat capacity is the mass specific heat (C) for the single crystal. In calculating FoMs, the mass specific heat capacity should be transformed into the volumetric specific heat capacity ($C_P = C \times \rho$, where $\rho = 7.45\,\text{g cm}^{-3}$ is the density of the CLT crystal).

3.4. Pyroelectric coefficient

Figure 4(a) shows the pyroelectric coefficient of all the samples over a wide temperature range from 50 °C–250 °C. In general, when the working temperature is far below the Curie point, pyroelectric coefficients gradually rise with the temperature. More interestingly, when the doping concentration is below the threshold concentration of 4 mol%, the pyroelectric coefficient decreases significantly from the undoped crystal. However, when the MgO concentration approaches 4 mol%, the corresponding pyroelectric coefficient presents a huge improvement. Furthermore, as the doping concentration exceeds 4 mol%, the pyroelectric coefficient decreases again.

3.5. Dielectric property

The relative permittivities of seven samples in various temperature ranges (from 50 °C–350 °C) and frequency ranges (from 0.1–100 kHz) are shown in figure 4(b). One can easily see that the seven permittivity curves increase with temperature and decrease with frequency. The dielectric drops with the increase of doping concentration from CLT to 3-LT. However, in 4-LT, the relative permittivity shows an obvious increase, and then, as the doping concentrations reach 5 and 6 mol%, the permittivity decreases sharply.

In the majority of research of FoMs, dielectric constants are recorded at 1 kHz [11, 26]. Thus, in this paper, the dielectric loss (tanδ) of all the samples is measured at 1 kHz. As presented in figure 4(c), the tanδ curves of the seven samples are similar and are close to zero below 200 °C. However, at high working temperature, they increase and separate. Specifically, at high temperature, the dielectric loss decreases with the rising MgO concentration (from 0 to 3 mol%), and then, reaches the highest value in 4-LT. After that, from 5 to 6 mol%, the dielectric loss decreases again.

3.6. Discussion of electrical parameters

A consideration of the MgO substitution process in CLT single crystal, as reflected in the IR and UV spectra in figure 2, could explain the variation of electrical parameters offered in figure 4. According to the Li-vacancy model [27]: some Ta^{5+} ions occupy Li sites and form anti-site (Ta_{Li}^{4+}) defects, where one Ta_{Li}^{4+} will require the introduction of four Li vacancies (V_{Li}^{-}) to maintain charge balance [28]. Specifically, in doped samples, the substitution of Mg^{2+} for Li^{+} and Ta^{5+} will vary the spontaneous polarization in different ways, and significantly influence the pyroelectric coefficient [29]. Meanwhile, high ionic polarizability will induce strong distortions of the oxygen octahedron and results in a large dipole moment [30], which increases the dielectric susceptibility (χ) and dielectric coefficient ($\varepsilon_r = 1 + \chi$), and vice versa [31, 32].

In figure 2(a), the initial IR transmission peak (in 3485 cm^{-1}) can be attributed to the V_{Li}–OH complex, which consists of Li vacancies and H^+ ions from H_2O molecules in the air [33]. For the case of 0 to 3 mol% Mg-doping, the IR shift (to longer wavelengths) could be explained by the weaker repelling force of Mg_{Li}^{+} than Ta_{Li}^{4+} to H^+ ions. At the same time, the UV edge in figure 2(b) is determined by the valence electron transition energy from the 2p orbital of O^{2-} to the 5 d orbital of Ta^{5+}. The order of polarizability ($Ta^{5+} > Mg^{2+} > Li^{+}$) suggests that the blueshift of UV edge could be due to the substitution for Ta^{5+}, which broadens the band gap of valence electron transition [34, 35]. Thus, an initial occupation process (where Mg substitutes for the Ta at the Li site, $Ta_{Li}^{4+} \rightarrow Mg_{Li}^{+}$) would weaken the spontaneous polarization and the dipole moment of oxygen octahedron (from $Ta_{Li}O_6$ to $Mg_{Li}O_6$ octahedron), which would decrease the corresponding pyroelectric coefficient and dielectric susceptibility. Then, from 3 to 4 mol%, the redshift of UV edge could be due to the substitution of Li^+ ions ($Li_{Li} \rightarrow Mg_{Li}^{+}$). Now, the stronger polarizability of the substitution ion would enhance the spontaneous polarization. In addition, the dipole moment of the oxygen octahedron is enhanced from $Li_{Li}O_6$ to $Mg_{Li}O_6$. These improvements result in an increased pyroelectric coefficient and relative permittivity. After that, as shown in figures 2(a) and (b), when the doping concentration exceeds 4 mol%, the blueshift of UV edge implies the extra Mg^{2+} starts to replace normal Ta sites, and the IR shift (to shorter wavelength) is attributed to the stronger attraction of Mg_{Ta}–OH complexes to H^+ ions. Again, due to the polarizability difference between Mg^{2+} and Ta^{5+}, this substitution ($Ta_{Ta} \rightarrow Mg_{Ta}^{3-}$) will reduce the spontaneous polarization and dipole moment (from $Ta_{Ta}O_6$ to $Mg_{Ta}O_6$ octahedron), and so will reduce the corresponding pyroelectric coefficient and relative permittivity.

Comparing light and heavy doping processes, the permittivity varies with different doping concentrations. This could be explained by the huge difference between $Ta_{Li}O_6$ and $Ta_{Ta}O_6$ octahedrons in the perovskite-like LT structure. Specifically, along the z-axis, one $Ta_{Li}O_6$ locates between two normal Ta ions. Under light doping, Mg occupation will break the symmetry of Ta_{Ta}–Ta_{Li} and form Ta_{Ta}–Mg_{Li}. Obviously, the newly formed asymmetric structure enhances the dipole moment. Considering the influence of both the oxygen octahedron and Ta/Li/Ta complex to Mg occupation, the reduction of permittivity is limited. However, in heavy doping process, the complex behaves differently. Since $Ta_{Ta}O_6$ is located between Li ions, Mg occupation dramatically reduces the asymmetry from Li_{Li}–Ta_{Ta} to Li_{Li}–Mg_{Ta} structure. Thus, in this case, the dopant decreases the permittivity significantly.

3.7. Figures of merit

After measuring and analyzing the specific heat capacity, pyroelectric coefficient, relative permittivity and dielectric loss, finally, two types of FoMs (F_V, F_D) can be calculated via equations (1) and (2). Figures 5(a) and (b) show the F_V and F_D of seven samples at different working temperatures, respectively. Since pyroelectric and dielectric properties are affected dramatically by temperature and dopant, the F_V and F_D behave differently. Specifically, in figure 5(a), F_V decreases weakly when the doping concentration is below 3 mol%, then, it increases and reaches the highest value in 5-LT. Also, due to the crucial effect of temperature on dielectric property and pyroelectric coefficient, the value of F_V increases with temperature. In particular, at high temperature, the F_V (5 mol%) is improved more than ten times to CLT. Then, from figure 5(b), we see that the initial Mg doping (ranges from 0–3 mol%) is detrimental to F_D. However, the F_D of 4-LT and 5-LT are nearly double that of CLT. Finally, as the doping concentration reaches 6 mol%, F_D decreases again. This wave-shaped F_D variation is mainly due to the competition between the dielectric and pyroelectric improvements. Table 1 shows the summary of the electrical parameters and FoMs for various pyroelectric materials. Obviously, the outstanding F_V and F_D for 5-LT represents remarkable potential pyroelectric device application. For instance, in our work, the F_V is 20 and 11 times greater than CLN and Zr:LN [22]. Compared with the newly produced Fe:KLTN single crystal [36], the F_V is enhanced 77 times. Moreover, even compared with PVDF, SBN-50 and TGS [11], the F_V of 5-LT shows

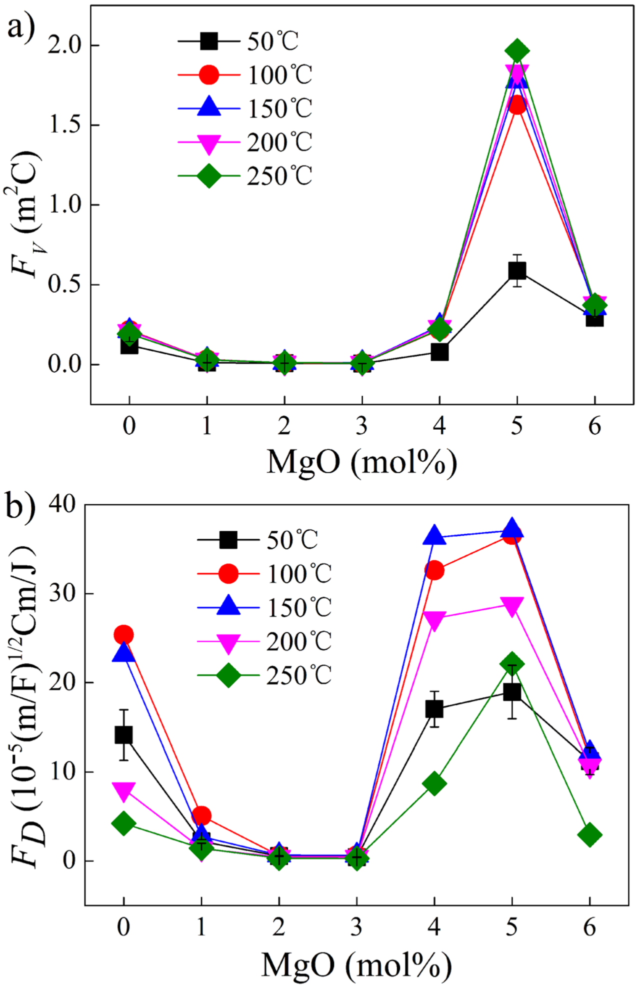

Figure 5. The voltage responsivity (F_V) and specific detectivity (F_D) versus various doping concentrations under different temperatures.

Table 1. Summary of electrical parameters and FoMs for kinds of pyroelectric materials. [11, 22, 36].

Material	p (10^{-4} C m^{-2} K^{-1})	ε_r	C_p (J cm^{-3} K^{-1})	T_C (°C)	F_V (m^2 C^{-1})	F_D (10^{-5} $(m/F)^{1/2}$ Cm/J)	Test condition
5 mol% Mg:LT	7.89	13	3.66	699.8	1.84	28.82	1 kHz, 200 °C
5 mol% Mg:LT	2.01	12	3.2	699.8	0.59	19	1 kHz, 50 °C
2 mol% Mg:LT	0.15	65	2.91	675.2	0.009	0.55	1 kHz, 50 °C
CLT	2.3	72	3.02	625.1	0.12	14	1 kHz, 50 °C
PVDF [11][a]	0.27	12	2.43	80	0.1	0.88	10 Hz, 50 °C
SBN-50 [11][b]	5.5	400	2.34	121	0.07	7.2	—
TGS [11][c]	5.5	55	2.6	49	0.43	6.1	1 kHz, 35 °C
CLN [22][d]	0.83	35	2.99	1140	0.09	2.8	1 kHz, 50 °C
Zr:LN [22][e]	0.85	22	2.63	—	0.167	18.7	1 kHz, 50 °C
Fe:KLTN [36][f]	6.65	—	2.7	97	0.024	0.85	100 kHz

[a] Polyvinylidence fluoride.
[b] $Sr_{0.5}Ba_{0.5}Nb_2O_6$, Strontium barium niobate.
[c] Triglycine sulphate.
[d] Congruent lithium niobate.
[e] 2 mol% zirconia doped congruent lithium niobate.
[f] Fe-doped niobium-rich potassium lithium tantalate niobate.

18, 26 and 4 times improvement, respectively. Similarly, with respect to specific detectivity, when compared with traditional pyroelectric materials such as PVDF, SBN-50 and TGS, the F_D is enhanced 33, 4 and 5 times [11]; compared with CLN and 2 mol% Zr:LN, the F_D of Mg:LT shows ten and twofold improvement [22]; and even 34 times more than Fe:KLTN [36]. These exciting improvements of FoMs prove the great potential of Mg:LT single crystals in pyroelectric transducers.

4. Conclusions

In conclusion, our work assesses the outstanding pyroelectric figures of merit of Mg:LT. The general tendency of permittivity and pyroelectric coefficient is revealed by the location analysis of MgO. Specifically, these intrinsic electrical parameters decrease with MgO doping from 0 to 3 mol%, but reach the highest value of 4 mol%, and then decrease again in more heavily doped samples. The 5 mol% Mg:LT single crystal provides the best FoMs (F_V and F_D), which are enhanced ten and twofold compared to undoped LT. Moreover, the positive effect of doping on Curie temperature also contributes to a broadening of the LT thermal application.

Acknowledgments

This work was supported by the National Natural Science Foundation of China (NSFC) (Nos. 11372361, 11302268, 11232015, 11472321, 11572355), the National Natural Science Foundation of Guangdong Province (2017A030310426, 2018A030313321), the Guangdong Science and Technology Project (2015B090927005) and the Fundamental Research Funds for the Central Universities (17lgpy37).

ORCID iDs

Yunzhong Zhu https://orcid.org/0000-0002-5229-822X

References

[1] Wang Z, Zhang J, Xu S, Wang L, Cao Z, Zhan P and Wang Z 2007 *J. Phys. D: Appl. Phys.* **40** 4482–4
[2] Fairley P D and Rutt H N 2000 *J. Phys. D: Appl. Phys.* **33** 2837–52
[3] Zhang W L, Yu Y C, Luo W B, Shuai Y, Pan X Q, Wu Q Q and Wu C G 2016 *Infrared Phys. Technol.* **80** 100–4
[4] Balakt A M, Shaw C P and Zhang Q 2016 *J. Mater. Sci.: Mater. Electron.* **27** 12947–54
[5] Dias C, Simon M, Quad R and Das-Gupta D K 1993 *J. Phys. D: Appl. Phys.* **26** 106–10
[6] Liu S T and Long D 1978 *Proc. IEEE* **66** 14–26
[7] Nye J F 1985 *Physical Properties of Crystals* (Oxford: Clarendon Press)
[8] Siegfried B and Bernd P 1990 *Ferroelectrics* **106** 393–8
[9] Hartley N P, Squire P T and Putley E H 1972 *J. Phys. E: J. Sci. Instrum.* **5** 787–9
[10] Chynoweth A G 1956 *J. Appl. Phys.* **27** 78–84
[11] Whatmore R W 1986 *Rep. Prog. Phys.* **49** 1335–86
[12] Suyal G and Setter N 2004 *J. Eur. Ceram. Soc.* **24** 247–51
[13] Lang S B and Ringgaard E 2012 *Appl. Phys.* A **107** 631–8
[14] Suyal G, Seifert A and Setter N 2002 *Appl. Phys. Lett.* **81** 1059–61
[15] Sinha N, Goel N and Singh B K 2012 *J. Solid State Chem.* **190** 180–85
[16] Abdullah K A, Batal M A, Hamdan R, Toni K, Zaraket J, Aillerie M and Salame C 2017 *Energy Proc.* **119** 545–55
[17] Wu C G, Sun X Y, Meng J, Luo W B, Li P, Peng Q X, Luo S Y and Shuai Y 2014 *Infrared Phys. Technol.* **63** 69–73
[18] Chopra S, Sharma S, Goel T C, Chatterjee R and Mendiratta R G 2006 *Comput. Mater. Sci.* **37** 134–40
[19] Nakamura K and Itagaki M 1994 *Jpn. J. Appl. Phys.* **33** 5404–6
[20] Chandramouli K and Koduri R 2009 *J. Mater. Sci.* **44** 1793–9
[21] Mangalam R V, Agar J C, Damodaran A R, Karthik J and Martin L W 2013 *ACS Appl. Mater. Interfaces* **5** 13235–41
[22] Zhu Y Z, Lin S P, Zheng Y, Ma D C and Wang B 2016 *J. Mater. Sci.* **51** 3155–61
[23] Shibata Y, Kuze N, Matsui M, Kanal M and Kawai T 1996 *Mat. Res. Soc. Symp. Proc.* **401** 273–8
[24] Kovacs L *et al* 1993 *J. Phys.: Condens. Matter* **5** 781–94
[25] Kumaragurubaran S, Takekawa S, Nakamura M and Kitamura K 2006 *J. Cryst. Growth* **292** 332–6

[26] Ehre D and Cohen H 2013 *Appl. Phys.Lett.* **103** 052901

[27] Iyi N, Kitamura K, Izumi F, Yamamoto J K, Hayashi T, Asano H and Kimura S 1992 *J. Solid State Chem.* **101** 340–52

[28] Kang X, Liang L, Song W, Wang F, Sang Y and Liu H 2016 *CrystEngComm* **18** 8136–46

[29] Xue D and Kitamura K 2003 *J. Cryst. Growth* **249** 507–13

[30] Li L, Zhu M, Zhou K, Wei Q, Zheng M and Hou Y 2017 *J. Appl. Phys.* **122** 204104

[31] Betancourt J, Saavedra-Arias J J, Burton J D, Ishikawa Y, Tsymbal E Y and Velev J P 2013 *Phys. Rev.* B **88** 085418

[32] Kandpal B and Upadhyay T C 2016 *IOSR J. Appl. Phys.* **8** 53–9

[33] Watanabe Y, Sota T, Suzuki K, Kitamura K and Kimura S 1995 *J. Phys.: Condens. Matter* **7** 3627–35

[34] Zhen X H, Zhao L C and Xu Y H 2003 *Appl. Phys.* B **76** 655–59

[35] Dai L, Yan Z, Jiao S, Xu C and Xu Y 2015 *RSC Adv.* **5** 36385–9

[36] Li Y, Li J, Zhou Z, Guo R and Bhalla A S 2013 *Europhys. Lett.* **104** 57008